PHYSICAL REVIEW B **78**, 174511 (2008)

Theory of nonequilibrium spin transport and spin-transfer torque in superconducting-ferromagnetic nanostructures

Erhai Zhao[1] and J. A. Sauls[2]
[1]*Department of Physics and Astronomy, University of Pittsburgh, Pittsburgh, Pennsylvania 15260, USA*
[2]*Department of Physics and Astronomy, Northwestern University, Evanston, Illinois 60208, USA*
(Received 4 September 2008; published 12 November 2008)

Spin transport currents and the spin-transfer torques in voltage-biased superconducting-ferromagnetic nanopillars (SFNFS point contacts) are computed. We develop and implement an algorithm based on the Ricatti formulation of the quasiclassical theory of superconductivity to solve the time-dependent boundary conditions for the nonequilibrium Green's functions for spin transport through the ferromagnetic interfaces. A signature of the nonequilibrium torque is a component perpendicular to the plane spanned by the two ferromagnetic moments. The perpendicular component is absent in normal-metal-ferromagnetic nanopillar contacts but is shown to have the same order of magnitude as the in-plane torque for nonequilibrium SFNFS contacts. The out-of-plane torque is due to the rotation of quasiparticle spin by the exchange fields of the ferromagnetic layers. In the ballistic limit the equilibrium torque is related to the spectrum of spin-polarized Andreev bound states, while the ac component, for small bias voltages, is determined by the nearly adiabatic dynamics of the Andreev bound states. The nonlinear voltage dependence of the nonequilibrium torque, including the subharmonic gap structure and the high-voltage asymptotics, is attributed to the interplay between multiple Andreev reflections, spin filtering, and spin mixing. These properties of spin angular momentum transport may be exploited to control the state of nanomagnets.

DOI: 10.1103/PhysRevB.78.174511 PACS number(s): 72.25.Mk, 74.50.+r

I. INTRODUCTION

Spin-polarized current passing through a ferromagnet (F) can transfer spin angular momentum to the ferromagnet and exert a torque on the magnetic moment.[1–4] This provides a mechanism for manipulating the state of nanomagnets. For example, magnetization precession and reversal driven by the spin-transfer torque has been observed in ferromagnet-normal-metal multilayers.[5,6] A promising multilayer geometry for device applications, such as random access memory and microwave oscillators, is the so-called "magnetic nanopillar" consisting of a ferromagnet-normal-metal-ferromagnet (FNF) trilayer connected to normal-metal (N) electrodes.[7,8] The typical thickness of each layer is several nanometers, and the diameter of the pillar is of the order of 50–100 nm.

Slonczewski[9] proposed a unified description of equilibrium and nonequilibrium spin-transfer torque in magnetic nanopillars based on the dynamics of the spin current. The spin current is not conserved across the ferromagnetic interface so the spin-transfer torque on each F layer equals the net spin flux it absorbs. In thermal equilibrium a persistent spin current flows in the N layer between the two ferromagnets. The spin current is related to the formation of spin-polarized states due to the spin-dependent confinement potential of the FNF trilayer.[10–12] The equilibrium current is responsible for the exchange torque between the two F layers. This torque prefers either parallel or antiparallel alignment of the magnetic moments depending on the thickness of the N layer.[13,14] Voltage biasing an FNF trilayer results in a nonequilibrium spin current in the N layer, as well as in the electrodes. The resulting torque on each F layer is proportional to the voltage.

A scattering theory for computing spin current and spin-transfer torque in normal-metal-ferromagnet hybrid structures was developed by several authors.[15–18] Within this approach the ferromagnetic layers are treated as sharp interfaces between normal conducting leads. Scattering matrices describing the transmission and reflection of electronic excitations, together with their spectra and distribution functions in the electrodes, determine the charge and spin transport.

Waintal and Brouwer[19,20] pointed out that spin angular momentum transfer acquires new features in magnetic nanopillars connected to superconducting (S) electrodes. For example, they showed that the nonequilibrium torque in NFNFS junctions may favor a perpendicular configuration of the two moments due to Andreev reflection at the NS interface for voltages below the superconducting gap, $eV<\Delta$.[19] They also showed that the equilibrium torque in SFNFS junctions depends on the condensate phase difference, ϕ, between the superconducting leads.[20] These features are consequences of energy-dependent phase-sensitive scattering of the electronic excitations at the ferromagnetic interfaces. Fabrication and control of superconducting-ferromagnetic nanopillars appears to be within the capability of current technology.[21] For example, the dc Josephson effect in SFNFS junctions has been reported in Ref. 21.

In order to better understand, design, and develop superconducting spin-transfer devices, a quantitative theory of spin transport and spin angular momentum transfer under nonequilibrium conditions is needed. In this paper we develop the theory of nonequilibrium spin transport and spin-transfer torque in voltage-biased SFNFS point contacts, i.e., superconducting nanopillars with diameter smaller than the superconducting coherence length of the electrodes. Under voltage bias, V, the phase difference, ϕ, increases with time at a rate given by the Josephson frequency, $\omega_J=2eV/\hbar$. In response, the spin current and spin-transfer torque oscillate

with time. In general, the time-dependent torque excites the ferromagnet by setting the magnetic moments into motion, which in turn affects the spin transport. A full theory of the coupled dynamics of the ferromagnetic moments and the spin current is outside the scope of this work. In this paper we assume the ferromagnetic moments do not change direction on the time scale set by the Josephson frequency, $T_J = 2\pi/\omega_J$. This assumption is justified for point contacts over a wide range of voltages because the characteristic frequency for the magnetization dynamics is set by the magnitude of the torque which scales linearly with the cross-sectional area of the contact, $\mathcal{A}$. For junctions with sufficiently large cross section, our assumption holds only for high-voltage bias. The quasistatic approximation eventually breaks down when the bias voltage is sufficiently small compared to the superconducting gap that the magnetization dynamics is comparable to or faster than the phase dynamics. Some aspects of this limit are discussed in Ref. 20.

Our theoretical approach is conceptually similar to the scattering theory for spin-transfer torque in normal-metal-ferromagnet hybrids.[15,16] We develop a scattering formulation for spin transport which includes the effects of particle-hole coherence arising from the superconducting leads. Our method is based on the Ricatti formulation of the quasiclassical theory of superconductivity[22–26] and is explained in Sec. II. We introduce the particle-hole coherence functions, the quasiparticle distribution functions and the boundary conditions obeyed by these functions at ferromagnetic interfaces. We also discuss the scattering matrices that describe the ferromagnetic interfaces; these matrices incorporate the key effects of spin-dependent scattering: *spin mixing and spin filtering*. In this section we also summarize the method we use to solve the interface boundary conditions. In Sec. III, we discuss the theory of the equilibrium torque in SFNFS contacts. We identify the microscopic scattering processes that give rise to the out-of-plane torque and derive an analytical result for the spin-transfer torque in terms of the spectrum of Andreev bound states at the point contact. In Sec. IV, we report results for the voltage, temperature, and misalignment angle dependences of the dc and ac components of the spin current and spin-transfer torque in voltage-biased SFNFS nanopillars. We summarize our results in Sec. V. Mathematical details of the solution of the time-dependent boundary conditions are presented in the Appendix.

II. THEORY

A powerful formalism to study time-dependent nonequilibrium transport in superconducting heterostructures is provided by the quasiclassical theory of superconductivity.[27,28] This theory describes phenomena on length scales larger than the Fermi wavelength, λ_f, and on time scales long compared to the inverse Fermi energy, $\hbar/E_f$. The central equations of the theory are a set of transport equations which govern the spatial and temporal variations of quasiclassical Green's functions. Strong localized potentials such as surfaces and interfaces are characterized by a scattering matrix, an interface "*S*-matrix," which defines the probability amplitudes for scattering between incident and outgoing normal-state particle and hole quasiparticles. The interface *S*-matrix is the key input to the boundary conditions for the quasiclassical Green's functions.[29–31]

Although these boundary conditions have been used to investigate the proximity effect and current-voltage characteristics of tunnel junctions and point contacts, their application has been somewhat limited.[32,33] The boundary conditions are nonlinear, possess spurious unphysical solutions which have to be discarded, and are time consuming to implement numerically under nonequilibrium conditions. An improved formulation of the quasiclassical boundary conditions was achieved by Eschrig[26] for nonmagnetic interfaces by reducing the boundary conditions for the quasiclassical Nambu-matrix propagators to boundary conditions for the particle-hole coherence functions, $\gamma^{R/A}$ and $\tilde{\gamma}^{R/A}$, and the distribution functions for the particlelike, x^K, and holelike, $\tilde{x}^K$, excitations (we follow the notation of Ref. 26). These components are 2×2 spin matrices defined on classical trajectories labeled by the Fermi velocity, $\mathbf{v}_f$, and are functions of spatial position, $\mathbf{R}$, Fermi momentum $\mathbf{p}_f$, excitation energy ϵ, and time, t. Note that pairs of particlelike and holelike components, e.g., $\tilde{q}$ and q, are related by the conjugation symmetry, $\tilde{q}(\mathbf{p}_f,\epsilon) = q^*(-\mathbf{p}_f,-\epsilon)$.

The equilibrium coherence functions determine the relative amplitude of normal-state particle and hole states that define the Bogoliubov excitations for the superconducting state. The pair of coherence functions also combine to determine local quasiparticle excitation spectrum, i.e., $N(\mathbf{p}_f,\epsilon) = \Re\mathfrak{e}[(1+\gamma^R\tilde{\gamma}^R)/(1-\gamma^R\tilde{\gamma}^R)]$. For nonequilibrium conditions and in the clean limit, the coherence functions also determine the probability amplitudes for branch conversion from electronlike to holelike quasiparticles and vice versa. The distribution functions determine the occupation probabilities for the particlelike and holelike excitations. We refer to both the coherence functions and distribution functions as Riccati amplitudes since all of these functions obey Riccati-type[35] differential equations.[22–26] These equations are supplemented by boundary conditions at an interface and by asymptotic conditions deep in the bulk electrodes. For our purposes a complete set of boundary conditions for the nonequilibrium Riccati amplitudes were recently derived for spin-active interfaces.[36,37] In contrast to the nonlinear boundary conditions for quasiclassical propagators[31] the boundary conditions for Riccati amplitudes are easier to solve and free of unphysical solutions. Thus, the Riccati formulation of quasiclassical theory provides an efficient method for finding the nonequilibrium Green's functions near spin-active interfaces.[36]

Several authors[25,38–41] have noted that caution must be exercised when applying the quasiclassical transport equations and related boundary conditions to multibarrier proximity structures even for structures with dimensions that are large compared to the Fermi wavelength. When there are multiple interfaces present the quasiclassical formulation can lead to errors that exceed the small expansion parameters that are the basis for the quasiclassical approximation, i.e., $1/k_f\xi_0 \ll 1$. This breakdown of quasiclassical approximation is believed due to the formation of closed trajectories that give rise to constructive quantum interference terms resulting from scattering (for normal-state quasiparticles) by several

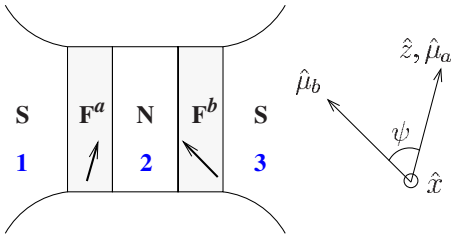

FIG. 1. (Color online) Schematic of superconducting magnetic nanopillar. The left electrode, middle spacer, and right electrode are also called region 1, 2, and 3, respectively. The two ferromagnetic layers are labeled by indices a and b. Their magnetization directions, $\hat{\mu}_a$ and $\hat{\mu}_b$, are in general misaligned; $\hat{\mu}_a$ is along the z axis, while $\hat{\mu}_b$ is at polar angle ψ in the yz plane. The x axis is along $\hat{\mu}_a \times \hat{\mu}_b$, and the diameter of the pillar is $d \ll \xi_0$.

different interfaces which invalidates the normalization condition for quasiclassical Green's functions.[25,41] However, for layered structures with two interfaces the quasiclassical theory yields correct results for junctions with many transmission channels. The quantum interference effect characterized by channel-dependent phase factors averages out when summed over many conduction channels. This has been verified by comparing the results of quasiclassical theory and microscopic Bogoliubov–de Gennes or Gorkov theory on the dc Josephson effect in double barrier SINIS junctions (I stands for an insulator layer).[39–41] In Ref. 42, quasiclassical theory was applied to study nonequilibrium charge transport in diffusive double-barrier SINIS junctions by solving the boundary conditions at the two insulator interfaces. Our method of computing spin currents and the spin-transfer torque in magnetic nanopillars is analogous to that developed in Ref. 42. Given that magnetic nanopillars have many conduction channels,[15,16] the quasiclassical approach is justified.

In this article we apply the Riccati method to study time-dependent transport in superconducting-ferromagnetic nanopillars (SFNFS junctions). The junction geometry and coordinate system are shown in Fig. 1. Two single-domain nanoscale ferromagnets, F^a and F^b, are separated by a N spacer. The FNF trilayer is connected in a circuit with electrodes (S) made of conventional s-wave superconductors. The ferromagnetic interfaces, F^a and F^b, are characterized by their scattering matrices, $\mathbb{S}^a$ and $\mathbb{S}^b$, respectively, that couple normal-state excitations in adjacent electrodes.

For simplicity we assume the ferromagnets to be identical except that their magnetic moments are misaligned by an angle ψ. The thickness of each layer, as well as the diameter of each nanopillar, is assumed to be much smaller than the superconducting coherence length, $\xi_0 = \hbar v_f / 2\pi k_B T_c$, and the inelastic mean-free path, ℓ_{in}. These criteria are easily met, for example, with Al electrodes. The N layer thickness L is assumed to be larger than the Fermi wavelength but still thin compared to the superconducting coherence length, $\lambda_f \ll L \ll \xi_0$. We also assume the leads and the trilayer are in the clean limit and the scattering at F^a and F^b is specular. We choose the magnetization direction, $\hat{\mu}_a$, as the quantization axis (z axis) for spin. The magnetic moments, $\hat{\mu}_a$ and $\hat{\mu}_b$, span the yz plane, while the x axis is perpendicular to both $\hat{\mu}_a$ and $\hat{\mu}_b$. As discussed above, we assume $\hat{\mu}_a$ and $\hat{\mu}_b$ are static on the Josephson time scale, T_J.

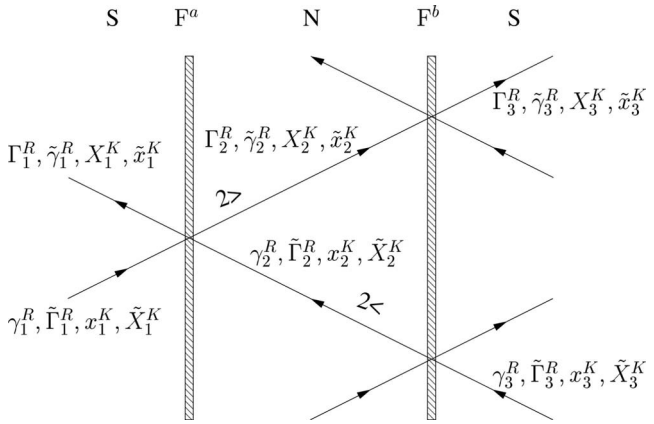

FIG. 2. Coupled scattering trajectories (directed lines) and the corresponding Riccati amplitudes for an SFNFS structure in the clean limit. The arrows indicate the direction of the Fermi momentum for quasiparticles defined on each trajectory. The right (left) going trajectories in the N region are labeled by 2> (2<).

Figure 2 shows the Riccati amplitudes defined on a set of scattering trajectories near the ferromagnetic interfaces. The Riccati amplitudes in the superconducting electrodes are classified into "incoming" Riccati amplitudes denoted by lower case symbols, $\{\gamma_j^{R,A}, \tilde{\gamma}_j^{R,A}, x_j^K, \tilde{x}_j^K\}$, and "outgoing" Riccati amplitudes denoted by upper case symbols, $\{\Gamma_j^{R,A}, \tilde{\Gamma}_j^{R,A}, X_j^K, \tilde{X}_j^K\}$, with $j=1,3$.[26,36] The amplitudes in the N region are also labeled in this way with incoming and outgoing groups defined with respect to the interface with F^a.

Proximity effects, i.e., the appearance of superconducting correlations in the N layer, as well as the suppression of superconductivity in the electrodes by the FNF trilayer, are encoded in the local particle-hole coherence functions. Charge and spin currents in each region, $i=1$, 2, and 3, are determined by the local distribution functions together with the coherence functions. For SFNFS junctions under a constant voltage bias the phase difference across the junction evolves according to the Josephson-Anderson relation, $\dot{\phi}(t) = \omega_J = 2eV/\hbar$. Thus, all local Riccati amplitudes defined above are time dependent. However, we can neglect spatial variations in the Riccati amplitudes within the N region. For example, the coherence function, Γ_2^R, in the N layer varies in space as $\Gamma_2^R(z') \sim \Gamma_2^R(0) e^{ik_T z'}$, where $k_T = 2\epsilon/v_f \ll k_f$ is the Tomasch wave vector and z' is the distance from F^a along trajectory 2>. Since z' is typically of the order of the N layer thickness (several nanometers) the phase accumulation $k_T z'$ is negligible except for grazing trajectories that are irrelevant for most transport phenomena across the trilayer. Similarly the distribution function, X_2^K, varies as $X_2^K(z') \sim X_2^K(0) e^{i\omega z'/v_f}$, where ω is of the order of the Josephson frequency $\omega_J \ll E_f$, and barely changes except for grazing trajectories. Thus, for thin N layers determining the local Riccati amplitudes is reduced to a simultaneous solution to the boundary conditions at F^a and F^b.

A. Boundary conditions

Boundary conditions at F^a and F^b connect the outgoing Ricatti amplitudes to the incoming Ricatti amplitudes via the

TABLE I. (Color online) Amplitudes for reflection and transmission of electrons and holes for the processes contributing to Eq. (1). h (e) stands for hole (electron), and $>$ ($<$) represents right (left) moving. For example, $1h> \rightarrow 1e<$ means a right-moving hole in region 1 converts into a left-moving electron in region 1.

Amplitude	Event	Diagram
Γ_1^R	$1h> \rightarrow 1e<$	
γ_1^R	$1h< \rightarrow 1e>$	
γ_2^R	$2h> \rightarrow 2e<$	
$\tilde{\gamma}_2^R$	$2e> \rightarrow 2h<$	
r_1^a	$1e> \rightarrow 1e<$	
t_1^a	$2e< \rightarrow 1e<$	

interface scattering matrices.[36] For voltage-biased junctions these boundary conditions describe the spin-dependent inelastic reflection and transmission of quasiparticles, loosely referred to as "multiple Andreev reflection" (MAR).[34] The summation of the multiple-scattering processes are contained in the boundary conditions, which for the retarded Ricatti amplitudes are

$$\Gamma_1^R = r_1^a \circ \gamma_1^R (\underline{S}_{11}^a)^\dagger + t_1^a \circ \gamma_2^R (\underline{S}_{12}^a)^\dagger, \tag{1}$$

$$\Gamma_2^R = r_2^a \circ \gamma_2^R (\underline{S}_{22}^a)^\dagger + t_2^a \circ \gamma_1^R (\underline{S}_{21}^a)^\dagger, \tag{2}$$

$$\gamma_2^R = r_2^b \circ \Gamma_2^R (\underline{S}_{22}^b)^\dagger + t_2^b \circ \gamma_3^R (\underline{S}_{23}^b)^\dagger, \tag{3}$$

$$\Gamma_3^R = r_3^b \circ \gamma_3^R (\underline{S}_{33}^b)^\dagger + t_3^b \circ \Gamma_2^R (\underline{S}_{32}^b)^\dagger. \tag{4}$$

Matrix multiplication in spin space is implied, and the $\circ$ operator denotes the folding product, which in the time domain is defined as,

$$[A \circ B](t_1,t_2) = \int_{-\infty}^{+\infty} dt\, A(t_1,t) B(t,t_2). \tag{5}$$

These boundary conditions can be expressed in terms of a set of rules for computing the branch-conversion scattering amplitudes near the interface. Table I lists the scattering amplitudes that determine the outgoing Ricatti amplitude, Γ_1^R, for electrode 1. This is the amplitude for retroreflection by the interface with branch conversion from a holelike to a particlelike excitation. The diagrammatic representation of the lowest-order elementary scattering processes that contribute to Γ_1^R are shown in Fig. 3.

The transmission (t) and reflection (r) amplitudes in Eqs. (1)–(4) are calculated from the normal-state, branch-conserving scattering amplitudes ($S_{ij}^{a/b}, \underline{S}_{ij}^{a/b}$), and elementary branch-conversion amplitudes ($\gamma_j^R, \tilde{\gamma}_j^R$) by summing the amplitudes for all multiple-scattering processes. In particular,

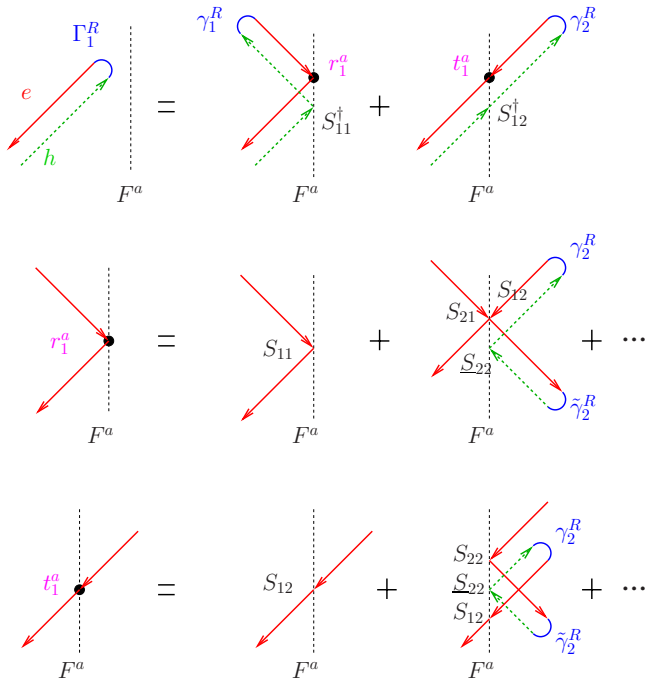

FIG. 3. (Color online) Diagrams for interface scattering with branch conversion from hole to particle. The full scattering amplitude includes Andreev reflection and transmission with branch conversion to all orders in the normal-state transmission (S_{12}, S_{21}) and reflection amplitudes (S_{11}, S_{22}).

for transmission and reflection from the central electrode (2) through $\mathrm{F}^{a/b}$,

$$t_2^a = [(S_{21}^a)^\dagger - \beta_{11}^a \circ (\beta_{12}^a)^{-1} (S_{22}^a)^\dagger]^{-1}, \tag{6}$$

$$r_2^a = -t_2^a \circ \beta_{11}^a \circ (\beta_{12}^a)^{-1}, \tag{7}$$

$$t_2^b = [(S_{23}^b)^\dagger - \beta_{33}^b \circ (\beta_{32}^b)^{-1} (S_{22}^b)^\dagger]^{-1}, \tag{8}$$

$$r_2^b = -t_2^b \circ \beta_{33}^b \circ (\beta_{32}^b)^{-1}, \tag{9}$$

where the coefficients β_{ij}^a are defined by

$$\beta_{ij}^a = (S_{ij}^a)^\dagger - \gamma_j^R (\underline{S}_{ij}^a)^\dagger \circ \tilde{\gamma}_i^R, \tag{10}$$

$$\tilde{\beta}_{ij}^a = \underline{S}_{ji}^a - \tilde{\gamma}_j^R \underline{S}_{ji}^a \circ \gamma_i^R, \quad i,j = 1,2. \tag{11}$$

The coefficients for interface F^b, β_{ij}^b, and $i=2,3$, are defined similarly. Notice that Γ_2^R and $\tilde{\Gamma}_2^R$ are the incoming amplitudes with respect to F^b so γ_2^R and $\tilde{\gamma}_2^R$ in Eqs. (10) and (11) should be replaced by Γ_2^R and $\tilde{\Gamma}_2^R$ in the definition of β_{ij}^b. Expressions for t_1^a and r_1^a are obtained from Eqs. (6) and (7) by index exchange $1 \leftrightarrow 2$, while t_3^b and r_3^b are obtained from Eqs. (8) and (9) by index exchange $2 \leftrightarrow 3$. The boundary conditions for the remaining coherence functions, such as $\tilde{\Gamma}_2^R$ and $\tilde{\gamma}_2^R$, are straightforward to write down by evoking particle-hole symmetry and are not listed here.[36]

The left and right side conducting leads are coupled through the FNF trilayer. Thus, Ricatti amplitude for one lead depends on elementary scattering processes that couple

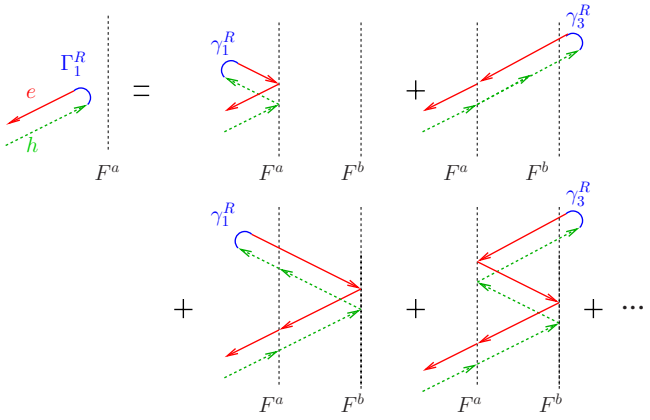

FIG. 4. (Color online) Elementary scattering processes contributing to Γ_1^R originating from transmission and reflection from both interfaces of the FNF trilayer.

excitations between leads 1 and 3. For example, Γ_1^R for lead 1 involves the summation of multiple-scattering processes from both interfaces. Low-order processes are shown in Fig. 4 which include transmission and reflection from both interfaces. Note that the processes that couple lead 1 to 3 are contained in Eqs. (1)–(9).

Boundary conditions for the distribution functions are also expressed in terms of the dressed reflection and transmission amplitudes,

$$X_1^K = r_1^a \circ x_1^K \circ \bar{r}_1^a + t_1^a \circ x_2^K \circ \bar{t}_1^a - a_1^a \circ \tilde{x}_2^K \circ \bar{a}_1^a, \tag{12}$$

$$X_2^K = r_2^a \circ x_2^K \circ \bar{r}_2^a + t_2^a \circ x_1^K \circ \bar{t}_2^a - a_2^a \circ \tilde{x}_1^K \circ \bar{a}_2^a, \tag{13}$$

$$x_2^K = r_2^b \circ X_2^K \circ \bar{r}_2^b + t_2^b \circ x_3^K \circ \bar{t}_2^b - a_2^b \circ \tilde{x}_3^K \circ \bar{a}_2^b, \tag{14}$$

$$X_3^K = r_3^b \circ x_3^K \circ \bar{r}_3^b + t_3^b \circ X_2^K \circ \bar{t}_3^b - a_3^b \circ \tilde{X}_2^K \circ \bar{a}_3^b. \tag{15}$$

However, the distribution functions also depend on the Andreev transmission amplitudes, i.e., transmission with branch conversion,

$$a_1^a = (\Gamma_1^R S_{12}^a - S_{12}^a \gamma_2^R) \circ (\tilde{\beta}_{22}^a)^{-1}, \tag{16}$$

$$a_2^a = (\Gamma_2^R S_{21}^a - S_{21}^a \gamma_1^R) \circ (\tilde{\beta}_{11}^a)^{-1}, \tag{17}$$

$$a_2^b = (\gamma_2^R S_{23}^b - S_{23}^b \gamma_3^R) \circ (\tilde{\beta}_{33}^b)^{-1}, \tag{18}$$

$$a_3^b = (\Gamma_3^R S_{32}^b - S_{32}^b \Gamma_2^R) \circ (\tilde{\beta}_{22}^b)^{-1}. \tag{19}$$

They are related to t and r by a set algebraic identities.[36] For example, the amplitude a_1^a describing the event $2h <\!\!\rightarrow 1e <$ is related to r_1^a by $r_1^a = S_{11}^a - a_1^a \tilde{\gamma}_2^R S_{21}^a$. Note that both "retarded" amplitudes, r, t, and the corresponding "advanced" counterpart, denoted by $\bar{r}, \bar{t}$, enter the boundary conditions for the distribution functions. These advanced functions are related to their retarded counterparts by symmetry, i.e., $\bar{q}(\epsilon, \epsilon') = q(\epsilon', \epsilon)^\dagger$.

B. Solution to the boundary conditions

The SFNFS nanopillars are small compared to the superconducting coherence length. This means that the suppression of the superconducting order parameter by the exchange fields of the ferromagnets, as well as the current flow, scales as $\sqrt{\mathcal{A}}/\xi_0$ and can be neglected. Also the voltage drop occurs essentially at the contact because of the large Sharvin resistance. Thus, the values of the incoming Riccati amplitudes in the exterior superconducting leads, $\{\gamma_j^R, \tilde{\gamma}_j^R, x_j^K, \tilde{x}_j^K, \ j = 1, 3\}$, are determined by the spectrum and distribution functions for bulk quasiparticle excitations in the left (1) and right (3) leads. Our task is then to solve the boundary conditions, Eqs. (1)–(19), for the Riccati amplitudes in the N layer and the outgoing Riccati amplitudes in the exterior leads.

We start with the coupled Eqs. (2) and (3), and solve them by an iterative method. Typically we are interested in the spin current in junctions with moderate to high transmission probabilities since otherwise the spin-transfer torque effect would be too small to be of interest. Therefore, a reasonable initial guess for Γ_2^R and γ_2^R is obtained by neglecting normal reflections at F^a and F^b. Thus, to zeroth order in $S_{jj}^{a/b}$, Eqs. (2) and (3) yield

$$\Gamma_2^R \simeq [(S_{21}^a)^\dagger]^{-1} \gamma_1^R (S_{21}^a)^\dagger, \tag{20}$$

$$\gamma_2^R \simeq [(S_{23}^b)^\dagger]^{-1} \gamma_3^R (S_{23}^b)^\dagger. \tag{21}$$

An improved approximation for Γ_2^R and γ_2^R is obtained by substituting the zeroth-order solution into the right side of Eqs. (2) and (3). After the coherence functions in the N layer are calculated, the outgoing coherence functions in the leads, Γ_1^R and Γ_3^R, are calculated from Eqs. (1) and (4). The transmission and reflection amplitudes (r, t, a) can then be evaluated from Eqs. (6)–(11) and (16)–(19). Each iteration of this procedure incorporates higher-order scattering processes. Operationally the iteration is stopped when the results for Γ_2^R and γ_2^R converge within a specified precision.

The linear equations for the distribution functions, X_2^K and x_2^K, Eqs. (13) and (14), are easily decoupled. For example, X_2^K obeys the equation,

$$X_2^K - c \circ X_2^K \circ \bar{c} = d, \tag{22}$$

with $c = r_2^a \circ r_2^b$ and

$$d = t_2^a \circ x_1^K \circ \bar{t}_2^a - a_2^a \circ \tilde{x}_1^K \circ \bar{a}_2^a + r_2^a \circ [t_2^b \circ x_3^K \circ \bar{t}_2^b - a_2^b \circ \tilde{x}_3^K \circ \bar{a}_2^b] \circ \bar{r}_2^a. \tag{23}$$

Equation (22) is solved iteratively to yield

$$X_2^K = \sum_{n=0}^{\infty} c^n \circ d \circ \bar{c}^n, \quad c^0 = 1. \tag{24}$$

For junctions of moderate to high transparency c is small, and the series summation converges rapidly. The other distribution functions in the N layer, $\tilde{X}_2^K$, x_2^K, and $\tilde{x}_2^K$, can be evaluated in a similar way. The distribution functions in the leads, X_1^K and X_3^K, are then calculated from Eqs. (12) and (15).

The main technical difficulty in implementing the iteration algorithm described above is the evaluation of the folding products. Following Ref. 43 we work in the energy domain. The folding products are then represented by products of infinite dimensional matrices for MAR. We truncate these MAR matrices to evaluate the folding products. Details of our analysis are provided in the Appendix.

The observable spin current is calculated from the quasiclassical Keldysh Green's functions. These functions can be constructed from the solutions for the Riccati amplitudes,[26]

$$\hat{g}^K = \begin{pmatrix} g^K & f^K \\ -\tilde{f}^K & -\tilde{g}^K \end{pmatrix} = -(2\pi i)\zeta^R \begin{pmatrix} x^K - \gamma^R \tilde{x}^K \tilde{\gamma}^A & x^K \gamma^A - \gamma^R \tilde{x}^K \\ \tilde{x}^K \tilde{\gamma}^A - \tilde{\gamma}^R x^K & \tilde{x}^K - \tilde{\gamma}^R x^K \gamma^A \end{pmatrix} \zeta^A, \quad (25)$$

where $\zeta^{R,A} = \mathrm{diag}[(1-\gamma^{R,A}\tilde{\gamma}^{R,A})^{-1}, -(1-\tilde{\gamma}^{R,A}\gamma^{R,A})^{-1}]$. In particular, the spin current in the N layer is given by

$$\vec{I} = N_f v_f \mathcal{A} \int_0^{\pi/2} \frac{d\Theta \sin 2\Theta}{4} \int \frac{d\epsilon}{2\pi i} \mathrm{Tr}\left\{ \frac{\hbar}{2} \vec{\sigma} [g^K_{2>} - g^K_{2<}] \right\}, \quad (26)$$

where the trajectories are indicated in Fig. 1 and $\Theta = \arccos(\hat{\mathbf{v}}_f \cdot \hat{\mathbf{m}})$ is the angle between the Fermi velocity and the interface normal $\hat{\mathbf{m}}$ at F^a, $\vec{\sigma} = (\sigma_x, \sigma_y, \sigma_z)$ are the Pauli spin matrices, and $\mathrm{Tr}\{\ldots\}$ denotes a trace over spin states.

C. Interface $\mathbb{S}$ matrix

The key inputs to our theory are the scattering matrices of the ferromagnetic layers, $\mathbb{S}^a$ and $\mathbb{S}^b$. In principle, these matrices can be calculated from *ab initio* microscopic theory.[44] However, the more efficient procedure is to fit a few key transport measurements to theoretical predictions based on models for $\mathbb{S}^{a/b}$. Thus, we proceed by carrying out calculations with basic models for the $\mathbb{S}^{a/b}$ matrices which capture the key features of spin-active scattering at ferromagnetic interfaces, i.e., spin filtering and spin mixing. More detailed discussions on the interface $\mathbb{S}$ matrix can be found in Ref. 36.

We parametrize $\mathbb{S}^{a/b}$ in terms of spin-dependent transparencies, $D_\uparrow$ and $D_\downarrow$, and a spin mixing angle, ϑ.[36] In particular, for interface F^a,

$$\mathbb{S}^a = \begin{bmatrix} S^a_{11} & S^a_{12} \\ S^a_{21} & S^a_{22} \end{bmatrix} = \begin{bmatrix} e^{-i\phi} S_r & i S_t \\ i S_t & e^{i\phi} S_r \end{bmatrix}. \quad (27)$$

The factors, $e^{\pm i\phi}$, with $\phi = k_f L/(\hat{\mathbf{p}}_f \cdot \hat{\mathbf{m}})$, describe the phase of normal-state quasiparticles propagating through the N layer,[45] while the normal-state spin-dependent reflection and transmission matrices $S_{r,t}$ are given by

$$S_r = \begin{bmatrix} \sqrt{R}_\uparrow e^{i\vartheta/2} & 0 \\ 0 & \sqrt{R}_\downarrow e^{-i\vartheta/2} \end{bmatrix}, \quad (28)$$

$$S_t = \begin{bmatrix} \sqrt{D}_\uparrow e^{i\vartheta/2} & 0 \\ 0 & \sqrt{D}_\downarrow e^{-i\vartheta/2} \end{bmatrix}. \quad (29)$$

The reflection and transmission probabilities for the two spin eigenstates are related by $R_\alpha = 1 - D_\alpha$ for $\alpha = \uparrow, \downarrow$, defined with respect to the polarization axis $\hat{\mu}_a$ of interface F^a. The nonequilibrium spin-transfer torque in normal-state magnetic nanopillars is predominantly determined by the spin filtering effect, i.e., $D_\uparrow \neq D_\downarrow$.[1,2,15,16,18] As we show below, spin mixing becomes important for the nonequilibrium torque in superconducting magnetic nanopillars. The spin mixing angle, ϑ, measures the relative phase shift between spin-up and spin-down electrons upon transmission or reflection; ϑ is easily shown to be the angle of rotation of the electron spin polarization around the magnetization direction after the electron is transmitted or reflected. This process is analogous to Faraday rotation in optics, and in the case of superconducting leads contribute to the torque on the ferromagnet. Note that for simplicity we assume the spin mixing angle for reflection and transmission are the same. This is a feature of models of the F layer which possess inversion and time-reversal symmetry (including the inversion of the magnetic moment), see Ref. 36.

Since we assumed that F^b and F^a are equivalent except for the orientation of their moments we can obtain the S-matrix for contact F^b, from $\mathbb{S}^a$ simply by rotating the ferromagnetic moment by angle ψ with respect to the x axis (see Fig. 1),

$$S^b_{22} = e^{i\phi} U(\psi) S_r U(\psi)^\dagger, \quad S^b_{33} = e^{-2i\phi} S^b_{22}, \quad (30)$$

$$S^b_{23} = S^b_{32} = i U(\psi) S_t U(\psi)^\dagger, \quad (31)$$

where $U(\psi) = e^{-i\sigma_x \psi/2}$ is the appropriate spin rotation operator. We also note that the scattering matrices for holes are also related to the scattering matrices for electrons by symmetry relations,[31] $S^{a/b}_{ij}(\mathbf{p}_\parallel) = [S^{a/b}_{ji}(-\mathbf{p}_\parallel)]^T$, where the superscript T denotes the transpose of a spin matrix and $\mathbf{p}_\parallel = \mathbf{p}_f - (\mathbf{p}_f \cdot \hat{\mathbf{m}})\hat{\mathbf{m}}$.

In general the values of $\{D_\uparrow, D_\downarrow, \vartheta\}$ depend on the quasiparticle trajectory $(\hat{\mathbf{p}}_f)$, the specific ferromagnetic material and the thickness of the F layers. For example, estimates for the transparencies of the Cobalt layer in Co-Cu-Co nanopillars are $D_\uparrow \sim 0.7$ and $D_\downarrow \sim 0.3$.[16] We are most interested in spin-current transfer in relatively high transmission junctions and thus relatively weak ferromagnetic materials such as Permalloy.[8,21] We consider two representative sets of spin-dependent transparencies:

$$\text{(I)} \quad D_\uparrow = 0.81, \quad D_\downarrow = 0.64, \quad (32)$$

$$\text{(II)} \quad D_\uparrow = 0.95, \quad D_\downarrow = 0.60. \quad (33)$$

We allow the spin mixing angle to take values ranging between 0 and 2π, with $\vartheta = \pi$ corresponding to the strongest spin mixing. This is intended to model F layers of various thickness. To put these numbers into perspective, consider the delta function scattering model as an example of weak spin mixing. In this model, each F layer is approximated by spin-dependent delta function potentials of strength V_α for spin α. In terms of $\theta_\alpha \equiv \arctan[\hbar(\mathbf{v}_f \cdot \hat{\mathbf{m}})/V_\alpha]$, the transparencies are $D_\alpha = \sin^2 \theta_\alpha$, and the spin-mixing angle is given by $\vartheta = \theta_\uparrow - \theta_\downarrow = \arcsin\sqrt{D_\uparrow} - \arcsin\sqrt{D_\downarrow}$. Thus, for transparency model (I), the delta function barriers yield $\vartheta = 0.061\pi(11.0°)$, while for model (II), $\vartheta = 0.146\pi(26.3°)$.

In the S matrices defined in Eqs. (27)–(31), spin-flip scattering is absent since the ferromagnetic layers are treated as static macrospins (single-domain ferromagnets with homogeneous magnetization) which give rise only to elastic scattering of normal-state electrons and holes. Our model is in line with that of Refs. 16 and 20. However, our formalism can be generalized to extend beyond the static macrospin approximation and to take into account inelastic scattering and spin-flip processes. However, these considerations are outside the scope of this report.

D. Transparent spin mixing

In the special case where normal reflection and spin filtering at F^a and F^b are negligible, the boundary conditions are greatly simplified and can be solved analytically. The nearly transparent spin-active point contact, introduced in Ref. 20, highlights the effect of spin mixing on spin-current transport in magnetic nanopillars. As discussed in Ref. 36, this is a reasonable approximation if the F layers are made of metallic ferromagnets with exchange energy $h \ll E_f$. With this approximation, the normal-state electron scattering matrix of F^a is described by only one parameter, the spin-mixing angle,

$$\mathbb{S}^a = \begin{bmatrix} 0 & e^{i\hat{\sigma}_z\vartheta/2} \\ e^{i\hat{\sigma}_z\vartheta/2} & 0 \end{bmatrix}, \tag{34}$$

and the scattering matrix for F^b is given by $\mathbb{S}^b = U(\psi)\mathbb{S}^a U^\dagger(\psi)$.

For transparent interfaces, the boundary conditions for Riccati amplitudes simplify, and we easily obtain the coherence functions in the N layer,

$$\Gamma_2^R = e^{i\sigma_z\vartheta/2}\gamma_1^R e^{-i\sigma_z\vartheta/2}, \quad \tilde{\Gamma}_2^R = e^{-i\sigma_z\vartheta/2}\tilde{\gamma}_1^R e^{i\sigma_z\vartheta/2},$$

$$\gamma_2^R = e^{i\sigma_\psi\vartheta/2}\gamma_3^R e^{-i\sigma'_\psi\vartheta/2}, \quad \tilde{\gamma}_2^R = e^{-i\sigma'_\psi\vartheta/2}\tilde{\gamma}_3^R e^{i\sigma_\psi\vartheta/2}, \tag{35}$$

where $\sigma_\psi = \sigma_z \cos\psi - \sigma_y \sin\psi$ and $\sigma'_\psi = \sigma_{-\psi}$. Similarly we obtain the distribution functions in the N layer,

$$X_2^K = e^{i\sigma_z\vartheta/2}x_1^K e^{-i\sigma_z\vartheta/2}, \quad \tilde{X}_2^K = e^{-i\sigma_z\vartheta/2}\tilde{x}_1^K e^{i\sigma_z\vartheta/2},$$

$$x_2^K = e^{i\sigma_\psi\vartheta/2}x_3^K e^{-i\sigma_\psi\vartheta/2}, \quad \tilde{x}_2^K = e^{-i\sigma'_\psi\vartheta/2}\tilde{x}_3^K e^{i\sigma'_\psi\vartheta/2}. \tag{36}$$

III. EQUILIBRIUM TORQUE

The equilibrium torque in superconducting nanopillars with chaotic N spacers has been studied in detail in Ref. 20. Here we make explicit connections between the equilibrium torque and the Andreev bound states in ballistic junctions. The objective is to reveal the microscopic scattering processes responsible for the equilibrium spin current and to facilitate our subsequent discussion on nonequilibrium torque.

Analytical expressions for the equilibrium spin current for the N layer of the nearly transparent SFNFS nanopillar are obtained from the Riccati amplitudes. In particular, the equilibrium Keldysh Green's functions are simply related to the thermal distribution function and the retarded Green's functions for the trajectories $2<$ and $2>$, i.e., $\hat{g}_{2>}^R$ and $\hat{g}_{2<}^R$ so the spin current

$$\vec{I} = N_f v_f \mathcal{A}\frac{\hbar}{2}\int \frac{d\epsilon}{2\pi}\tanh\frac{\epsilon}{2T}\mathrm{Im}\langle \mathrm{Tr}[\vec{\sigma}(g_{2>}^R - g_{2<}^R)]\rangle, \tag{37}$$

where N_f is the density of states at the Fermi energy, v_f is the Fermi velocity, and $\langle\ldots\rangle \equiv \int_0^{\pi/2}\sin\Theta\cos\Theta(\ldots)d\Theta/2$ is the angular average over the Fermi surface, including the projection of the quasiparticle spin current along the interface normal, i.e., $\hat{\mathbf{m}}\cdot\hat{\mathbf{v}}_f = \cos\Theta$. The retarded Green's functions are easily constructed from the Riccati amplitudes given in Eq. (35). By inspecting the poles of $g_{2<}^R$, we observe that a pair of Andreev bound states form at subgap energies,

$$\epsilon_\pm^<(\phi) = \mathrm{sgn}\left[\sin\left(\frac{\phi \pm \chi}{2}\right)\right]\cos\left(\frac{\phi \pm \chi}{2}\right)\Delta, \tag{38}$$

with $\chi \equiv \arccos[1 - 2\sin^2\vartheta\cos^2(\psi/2)]$. For trajectory $2>$, the bound states are at $\epsilon_\pm^>(\phi) = \epsilon_\pm^<(-\phi)$. Thus, for a set of coupled scattering trajectories there are in general four bound states, $\{\epsilon_j^B, \quad j = 1,2,3,4\}$. These Andreev bound states are spin-polarized (cf. Ref. 46 for a discussion of spin-polarized Andreev bound states in SFIFS junctions). For example, the bound states with energies $\epsilon_\pm^<$ correspond to spin eigenstates polarized along the axis $\hat{\mathbf{n}} = (n_x, n_y, n_z)$,

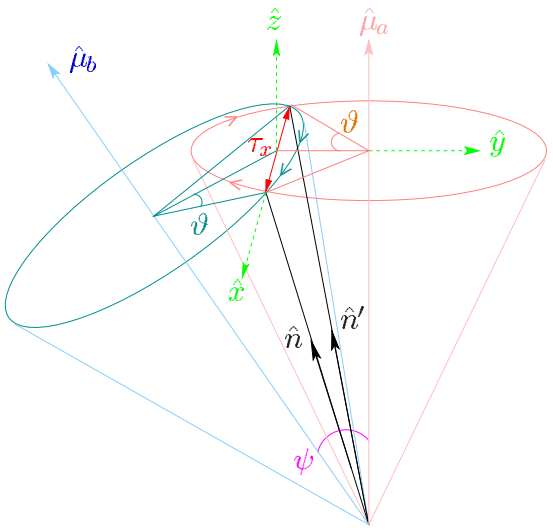

FIG. 5. (Color online) The round trip of the spin polarization of a left-moving electron in the N layer with energy $\epsilon_\pm^<$ and initially polarized along $\hat{\mathbf{n}}$. Upon traversing F^a to the left superconductor, $\hat{\mathbf{s}}$ is rotated from $\hat{\mathbf{n}}$ by $-\vartheta$ around $\hat{\mu}_a$. After the Andreev reflection at the left superconductor, the retroreflected hole passes through F^a again so that $\hat{\mathbf{s}}$ is rotated by another $-\vartheta$ around $\hat{\mu}_a$ and arrives at $\hat{\mathbf{n}}'$. As a result, spin angular momentum $\vec{\tau}_a = (\hat{\mathbf{n}} - \hat{\mathbf{n}}')\hbar/2$ is transferred to F^a, which as shown is along the x direction. The right-moving hole passes through F^b and is retroreflected into an electron by the right superconductor. After the electron passes through F^b to get back in N, $\hat{\mathbf{s}}$ is rotated by -2ϑ around $\hat{\mu}_b$ and returns to $\hat{\mathbf{n}}$. The second half of the trip transfers spin angular momentum $\vec{\tau}_b = -\vec{\tau}_a$ to F^b.

$$\hat{\mathbf{n}} = \left(\sin\frac{\psi}{2}\sin\,\vartheta, -\sin\frac{\psi}{2}\cos\,\vartheta, \cos\frac{\psi}{2}\cos\,\vartheta \right). \tag{39}$$

The Andreev bound states can be visualized as polarized electrons (holes) confined within the FNF trilayer by the superconducting pair potential of the two electrodes. Quasiclassically, these bound states correspond to excitations traversing closed trajectories between the superconducting leads. Consider an electron on trajectory $2<$, for example. In order to form a bound state, its energy has to be such that the total phase accumulation during a round trip, including the phase acquired while going through the F layers as well as that acquired during the Andreev reflection, is a multiple of 2π (the Bohr-Sommerfield quantization condition); additionally its spin has to be polarized along $\hat{\mathbf{n}}$ so that in one round trip its spin polarization returns to its original direction. The evolution of the spin polarization during one round trip is illustrated in Fig. 5. It follows from the geometry that the mutual torque between F^a and F^b is along the x direction.

In equilibrium the spin current only flows between the two F layers; it vanishes in the superconducting electrodes because the total spin of a Cooper pair is zero (here we only consider conventional s-wave spin-singlet superconductors). The net contribution from continuum states to the spin current in Eq. (37) is zero so the equilibrium spin current is carried entirely by the spin-polarized Andreev bound states. We carry out the integration over the spectrum using the residue theorem and find that the y and z components of the net spin current vanish and that the x component is directly related to the spectrum of bound states,

$$I_x = N_f v_f \mathcal{A}\pi\hbar \sum_{j=1}^{4} \left\langle \frac{\partial \epsilon_j^B}{\partial \psi} f(\epsilon_j^B) \right\rangle, \tag{40}$$

where $f(\epsilon) = 1/(e^{\epsilon/k_B T}+1)$ is the Fermi function. Written explicitly, the spin current in the N layer is given by

$$\vec{I}(\phi,\psi,T) = \hat{x}(N_f v_f \mathcal{A}\pi\hbar\Delta)\sin\,\psi \times \left\langle \frac{\sin^2\,\vartheta}{2\,\sin\,\chi} \sum_{\alpha=\pm 1} \sin\frac{\chi+\alpha\phi}{2} \tanh\left(\frac{\Delta}{2T}\cos\frac{\chi+\alpha\phi}{2} \right) \right\rangle. \tag{41}$$

Its magnitude is set by the scale $N_f v_f \mathcal{A}\Delta\hbar$, where Δ is the energy gap at temperature T. The dependence of the spin current on $\psi = \arccos(\hat{\mu}_a \cdot \hat{\mu}_b)$ is generally nonsinusoidal since χ is also a function of ψ. The mutual torque between the F layers, $\vec{\tau}_b = -\vec{\tau}_a = \vec{I} = \tau\hat{x}$, is along the x axis. Moreover if the moments were free to rotate, these torques would drive a mutual precession of $\hat{\mu}_a$ and $\hat{\mu}_b$.

A similar analysis for the equilibrium Josephson (charge) current, I_e, can be carried out with the result that I_e may be expressed in terms of the *phase dispersion* of the Andreev bound-state energies,

$$I_e = 2eN_f v_f \mathcal{A}\pi \sum_{j=1}^{4} \left\langle \frac{\partial \epsilon_j^B}{\partial \phi} f(\epsilon_j^B) \right\rangle. \tag{42}$$

It follows from Eqs. (40) and (42) that

$$\hbar\frac{\partial I_e}{\partial \psi} = 2e\frac{\partial \tau}{\partial \phi}. \tag{43}$$

This relation between the equilibrium spin-transfer torque and the Josephson charge current was previously written down in Ref. 16 using free-energy arguments. While this relation provides a nice check on our equilibrium results, it does not generalize to nonequilibrium charge and spin transport.

Equations (38)–(41) are the central results for the equilibrium spin current. We have explicitly shown that besides carrying Josephson supercurrent the Andreev bound states mediate a mutual torque in the x direction between the F layers. As shown in Fig. 5, finite spin mixing at the two F layers, i.e., rotation of the spin polarization by the exchange field, is crucial for producing the equilibrium spin-transfer torque. The analysis outlined above can be carried out for arbitrary SFNFS junctions with finite spin filtering. The details of the bound-state spectrum will be different, but Eqs. (38)–(41) remain valid.

The equilibrium spin-transfer torque in SFNFS junctions and NFNFN junctions share a similar origin. In both cases, the persistent spin-current flow can be traced to the formation of spin-polarized bound states and understood as a quantum interference phenomena. However, there is a major difference. In NFNFN structures, the spin current is rather fragile to mesoscopic fluctuations[16] and strongly suppressed by random impurity scattering. In reality, the exchange coupling between the F layers in a normal junction is effectively short ranged, for example, it vanishes for $L > 20$ nm.[47] By contrast, the spin current in high transmission superconducting junctions is robust against impurity scattering,[20] and the proximity-induced exchange coupling is long ranged. The long-range nature of the induced exchange field in superconductors by a proximity contact with a ferromagnet was studied in Ref. 48. As demonstrated in normal-metal-superconductor hybrid structures,[49,50] the phase coherence between incoming electrons and Andreev reflected holes persists throughout the diffusive normal metal for energies less than the Thouless energy. These low-energy excitations in the N layer can mediate exchange coupling between the F layers even when L is comparable to the superconducting coherence length.

IV. NONEQUILIBRIUM TORQUE

An applied voltage across an SFNFS junction leads to time-dependent nonequilibrium spin currents in the superconducting leads, as well as the interior normal-metal layer, i.e., currents in all regions of the trilayer, $\vec{I}^{(i)}(t)$, with $i \in \{1,2,3\}$. Since the Josephson phase is varying as $\varphi(t) = 2eVt/\hbar \equiv \omega_J t$ we can expand the currents in each layer in Fourier series defined by the Josephson frequency,

$$\vec{I}^{(i)}(t) = \vec{I}_0^{(i)}(V) + \sum_{k=1}^{\infty} [\vec{I}_{kc}^{(i)}(V)\cos(k\omega_J t) + \vec{I}_{ks}^{(i)}(V)\sin(k\omega_J t)]. \tag{44}$$

It follows that the spin-transfer torque on F^b, $\vec{\tau}^b(t) = \vec{I}^{(2)}(t) - \vec{I}^{(3)}(t)$, has the form

$$\vec{\tau}^b(t) = \vec{\tau}_0^b + \sum_{k=1}^{\infty} [\vec{\tau}_{kc}^b \cos(k\omega_J t) + \vec{\tau}_{ks}^b \sin(k\omega_J t)]. \tag{45}$$

For the coordinate system shown in Fig. 1, the dc torque $\vec{\tau}_0^b = \tau_{0x}^b \hat{\mathbf{x}} + \tau_{0y}^b \hat{\mathbf{y}} + \tau_{0z}^b \hat{\mathbf{z}}$ can be decomposed into the in-plane ($\parallel$) and out-of-plane ($\perp$) components,

$$\vec{\tau}_0^{b,\parallel} = \tau_{0y}^b \hat{\mathbf{y}} + \tau_{0z}^b \hat{\mathbf{z}}, \tag{46}$$

$$\vec{\tau}_0^{b,\perp} = \tau_{0x}^b \hat{\mathbf{x}}. \tag{47}$$

Note that both $\vec{\tau}_0^{b,\parallel}$ and $\vec{\tau}_0^{b,\perp}$ are perpendicular to $\hat{\mu}_b$. In what follows we discuss how the Fourier components of $\vec{\tau}_b$ depend on the voltage bias V, the spin mixing angle ϑ, and the misalignment angle ψ.

A. Dc spin current

Figure 6 shows the dc spin current for the N layer in the zero-temperature limit for the delta function scattering model with $D_\uparrow = 0.81$, $D_\downarrow = 0.64$, $\vartheta = 0.061\pi$, and $\psi = \pi/2$. Note that the spin current and spin-transfer torque are plotted in units of $N_f v_f \mathcal{A}\Delta(T)\hbar/2$ in all figures. We note two major differences between the nonequilibrium dc spin current in superconducting versus normal-state magnetic nanopillars. First, in normal-state nanopillars the spin current is linear in the bias voltage[16] (within the quasiclassical approximation), whereas for superconducting nanopillars the spin-current-voltage characteristics are highly nonlinear and possess subharmonic gap structure (SGS). Second, the spin current in normal-state nanopillars is predominately due to spin filtering and lies within the plane spanned by $\hat{\mu}_a$ and $\hat{\mu}_b$ (see Ref. 16). By contrast, in superconducting nanopillars, spin mixing is important; it controls the current-voltage characteristics of the in-plane spin current and leads to a finite out-of-plane spin current along $\hat{\mathbf{x}} = \hat{\mu}_a \times \hat{\mu}_b$. As shown in Fig. 6, the out-of-plane spin-current component, I_{0x}, is finite at $V=0$ and decays to zero at high voltages, $eV \gg \Delta$. On the other hand, the in-plane spin-current components, I_{0y} and I_{0z}, are zero at $V=0$ and grow linearly with V at high voltages.

The SGS of the spin current develops somewhat analogously to the SGS of dc charge current in voltage-biased Josephson junctions.[43,51–55] The SGS structure reflects the opening of additional channels (onsets) as well as resonances associated with multiple Andreev reflection (MAR) processes. The nth order MAR channel has an onset voltage $V_n = 2\Delta(T)/ne$. This transport mechanism is more efficient for charge transport since the Cooper pairs carry charge $2e$ but zero spin. A single MAR process may transport multiple units of charge but only one quantum of electron spin (as illustrated in Fig. 8). Nevertheless, the subgap spin current develops due to MAR and can be resonantly enhanced when a MAR trajectory in energy space intersects one of the FS surface bound states, the energy of which depends on the spin mixing angle.[37,55] This generates resonant transmission of the spin for voltages tuned to the bound-state energy.

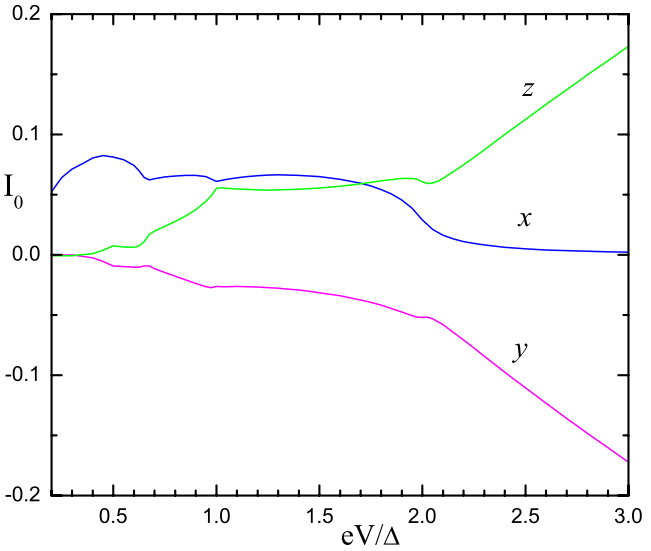

FIG. 6. (Color online) The x, y, and z components of dc spin current in the N layer for perpendicular configuration $\psi = \pi/2$. $D_\uparrow = 0.81$, $D_\downarrow = 0.64$, $\vartheta = 0.061\pi$, and $T=0$. The spin mixing is rather weak, and the subharmonic gap structures are close to voltage $V_n = 2\Delta/ne$. The unit for spin current is $N_f v_f A\Delta\hbar/2$.

For weak spin mixing shown in Fig. 6, the SGS exhibits singularities in the differential conductance (dI_0/dV) located approximately at V_n. Increasing the degree of spin mixing increases the magnitude of the current, eventually leading to reversal in the current direction and generally smoothes out the singularities. The spin current vanishes as the spin-mixing angle approaches π. Figure 7 shows the out-of-plane dc spin current in the N layer as a function of voltage for a range of spin mixing angles. For such high transmission junctions, the main contribution to I_{0x} comes from consecutive spin rotations when electrons (holes) undergo multiple Andreev reflection (Fig. 8). Roughly speaking, the total number of subgap MARs is inversely proportional to V; as a result I_{0x} decays rapidly at high voltages. The magnitude of I_{0x} also becomes small for ϑ close to 0 or π, where the quasiparticle spin direction is hardly changed in each Andreev reflection (see Fig. 5).

B. Dc spin-transfer torque

Once the spin current is known in each region, the torque on F^b is obtained by $\vec{\tau}^b = \vec{I}^{(2)} - \vec{I}^{(3)}$. Figure 9 shows the dc

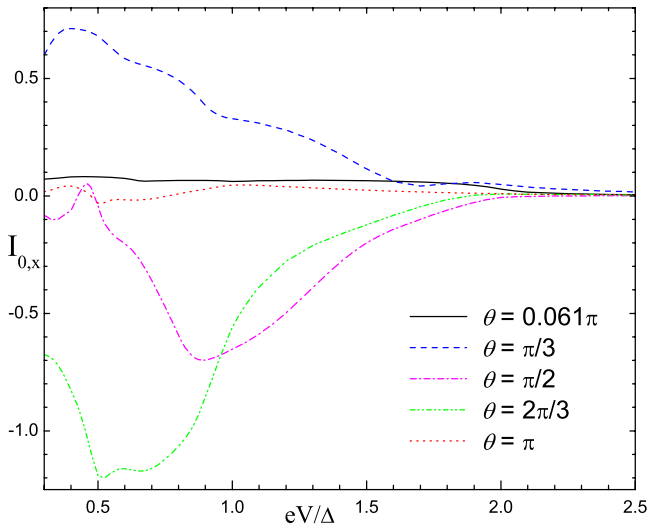

FIG. 7. (Color online) The x component of dc spin current in the N layer for $\psi=\pi/2$ and different spin mixing angles. $D_\uparrow=0.81$, $D_\downarrow=0.64$, and $T=0$.

torque on F^b as a function of the bias voltage for $D_\uparrow=0.95$, $D_\downarrow=0.6$, $\psi=\pi/2$, $T=0.5T_c$, and a variety of spin mixing angles. Note that the y component of $\vec{\tau}^b$ vanishes for $\psi=\pi/2$. We observe that the voltage dependence of the in-plane torque (τ^b_{0z}) and the out-of-plane torque (τ^b_{0x}) are sensitive to spin mixing and, more importantly, exhibit very different voltage characteristics. The in-plane torque vanishes for $V\to 0$, while the out-of-plane torque is finite at zero voltage. The out-of-plane torque varies more dramatically with the bias voltage for $V<2\Delta/e$, changing sign around 2Δ in the case of weak spin mixing (i.e., $\vartheta<\pi/3$). This marks the crossover from the low-voltage regime, where only high-order MAR processes with finite number of subgap Andreev reflections contribute to the spin momentum transfer, to the high-voltage regime, where direct transmission without Andreev reflection dominates the spin transport. Indeed, for $V\gg 2\Delta$, both components become linear in V; however, note that the magnitude of τ^b_{0z} (for $V\gg 2\Delta$) is suppressed from its

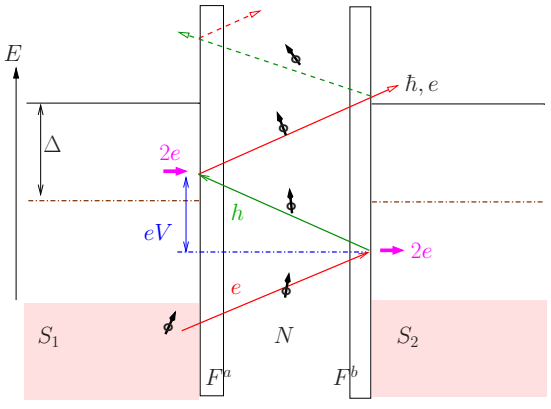

FIG. 8. (Color online) Schematic diagram illustrating the trajectory of a subgap excitation undergoing MAR. Charge transport occurs at each Andreev reflection, while spin is transported by the excitation with energy above the gap that escapes into the superconducting lead.

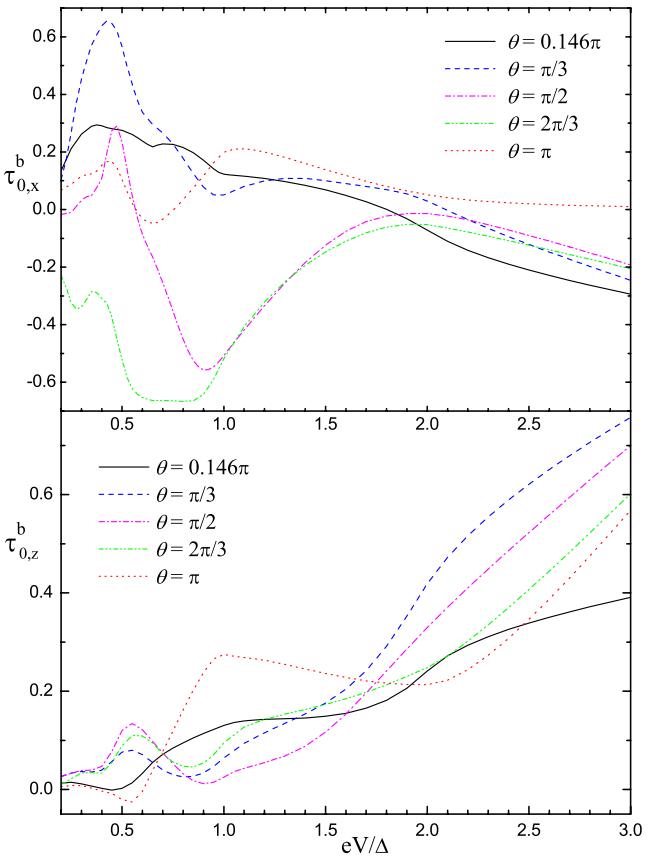

FIG. 9. (Color online) The dc torque on F^b in x (upper panel) and z (lower panel) directions for $\psi=\pi/2$ and different spin mixing angles. $D_\uparrow=0.95$, $D_\downarrow=0.6$, and $T=0.5T_c$.

normal-state value because of the superconducting gap in the excitation spectrum. Finally, we note that that if we scale the torque in units of $N_f v_f \mathcal{A}\Delta(T)\hbar/2$ and the voltage in units of $\Delta(T)/e$ then both in-plane and out-of-plane components of the torque are nearly temperature independent.

The spin-transfer toque vanishes in the parallel and antiparallel configurations for the two F layers, i.e., $\psi=0$ and π. The functional forms for $\vec{\tau}^{b,\parallel}_0(\psi)$ and $\vec{\tau}^{b,\perp}_0(\psi)$ are generally complicated. Two calculations are shown in Fig. 10 for $\vartheta=2\pi/3$ and $\vartheta=\pi$ at voltage $V=1.5\Delta/e$, with $D_\uparrow=0.81$, $D_\downarrow=0.64$, and $T=0.5T_c$. In the case of $\vartheta=2\pi/3$, the magnitude of out-of-plane torque is considerably larger than the in-plane torque, and it possesses a pronounced maximum around $\psi\simeq\pi/5$. In the case of $\vartheta=\pi$, however, the out-of-plane torque is of the same order as the in-plane torque, and it varies rather slowly with ψ. At higher voltage, $eV>2\Delta$, and weak spin mixing both the in-plane and out-of-plane torques vary approximately as $\sin\psi$, as shown in Fig. 11 for $\vartheta=0.061\pi$ and $V=2.5\Delta/e$. The high-voltage asymptotic behavior of $\vec{\tau}^{b,\parallel}_0(\psi)$ is similar to that of the normal-state magnetic nanopillars discussed in Ref. 16.

C. Ac spin-transfer torque

Figure 12 shows the first Fourier components of the ac torque on F^b, $\vec{\tau}_{1c}(V)$ and $\vec{\tau}_{1s}(V)$, for $D_\uparrow=0.95$, $D_\downarrow=0.6$, $\vartheta=0.146\pi$, $\psi=\pi/2$, and $T=0.5T_c$. The ac spin current comes

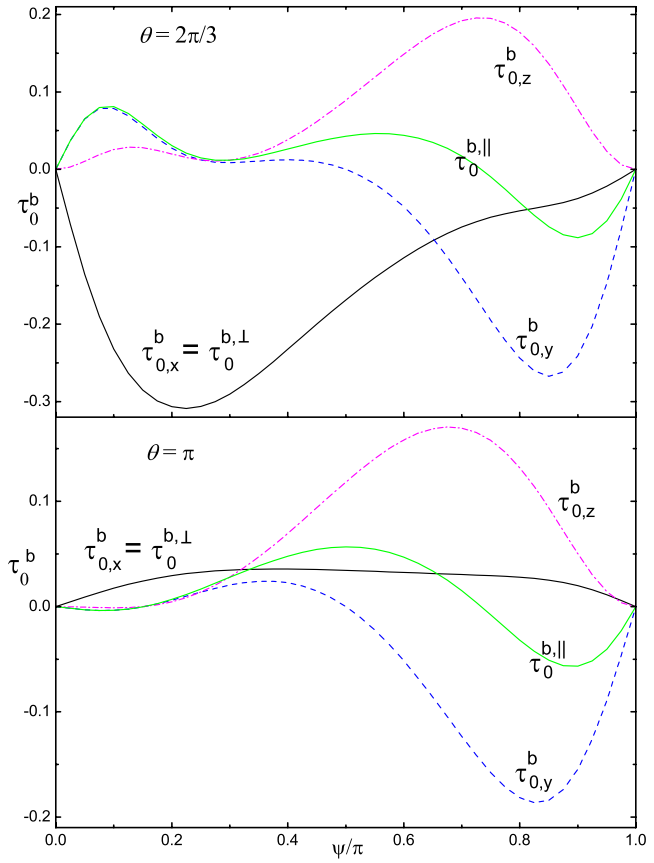

FIG. 10. (Color online) The dc torque on F^b as a function of misalignment angle ψ for strong spin mixing, $\vartheta=2\pi/3$ and π. $D_\uparrow=0.81$, $D_\downarrow=0.64$, $T=0.5T_c$, and $V=1.5\Delta/e$. The x, y, and z components of the dc torque are plotted separately. Also shown is the magnitude of the in-plane torque (labeled by "||"), the vector sum of the y and z components.

from the interference between MAR processes of different order. As a result, the ac torque rapidly decays to zero at high voltages. To get a better understanding of the ac torque, in what follows we derive its analytical expression for transparent SFNFS point contacts.

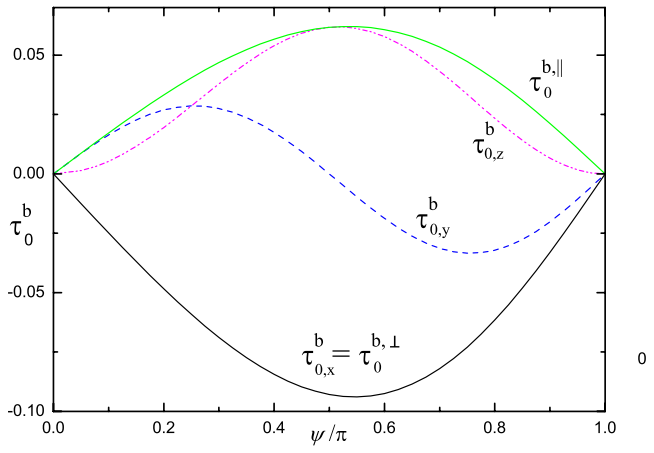

FIG. 11. (Color online) The dc torque on F^b as a function of misalignment angle ψ for weak spin mixing, $\vartheta=0.061\pi$, at high voltages, $V=2.5\Delta/e$. $D_\uparrow=0.81$, $D_\downarrow=0.64$, and $T=0.5T_c$.

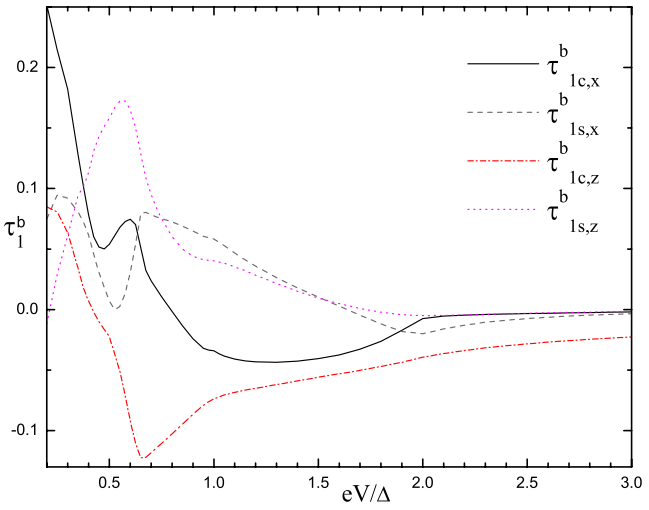

FIG. 12. (Color online) The first Fourier component of the ac torque on F^b. Shown are $\vec{\tau}_{1c}$ and $\vec{\tau}_{1s}$ in x and z directions (the y components are zero for $\psi=\pi/2$). $D_\uparrow=0.95$, $D_\downarrow=0.6$, $\vartheta=0.146\pi$ (weak spin mixing), $\psi=\pi/2$, and $T=0.5T_c$.

The nonequilibrium spin current in transparent point contacts can be computed directly from Eqs. (35) and (36). The analysis is carried out in the Appendix; the resulting expression for $\vec{I}^{(2)}$ is given by Eq. (A17). We observe that the dc spin current vanishes in all three regions, $i=1,2,3$. This is a feature of the nearly transparent interface model, and it shows that finite spin filtering is required for a nonzero dc torque. For the ac current the dominant contribution comes from the first Fourier component, $\vec{I}^{(i)}_{1c}(V)\cos(\omega_J t)+\vec{I}^{(i)}_{1s}(V)\sin(\omega_J t)$. The cosine term is negligible compared to the sine term when the inelastic rate is small; we have assumed $\Gamma_{in}=10^{-4}\Delta$. The sine component of the current vanishes in the superconducting leads; however $\vec{I}^{(2)}_{1s}$ is finite and polarized along the $\hat{\mathbf{x}}$. Thus, the time-dependent torque is

$$\vec{\tau}^b(t) = -\vec{\tau}^a(t) \simeq \tau_{1s}(V,T)\sin(\omega_J t)\hat{\mathbf{x}}. \tag{48}$$

From Eq. (A17), we found that the torque is proportional to $\sin^2\vartheta$ and $\sin\psi$,

$$\tau_{1s}(V,T) = N_f v_f \mathcal{A}\Delta(T)\frac{\hbar}{2}F(V,T)\langle\sin^2\vartheta\rangle\sin\psi. \tag{49}$$

The voltage dependence of $\vec{\tau}^b$ is given by the dimensionless function $F(V,T)$, plotted in Fig. 13 for $T=0.5T_c$ and $T=0$. Since $F(V,T)$ depends weakly on T, the temperature dependence of $\vec{\tau}_b$ is mainly determined by the gap $\Delta(T)$.

Note that the ac torque decays monotonically with voltage in transparent contacts. This is in sharp contrast with the ac torque, $\tau^b_{1s}(V)$, shown in Fig. 12 for $D_\alpha<1$. In this case resonant MAR leads to sharp structure in $\tau^b_{1s}\hat{\mathbf{x}}$ for $V<2\Delta$. At high voltage, $eV\gg\Delta$, the dominant contribution to spin current comes from the lowest-order MAR processes, i.e., the terms $m=0,1$ in Eq. (A17). Keeping only the leading-order terms we obtain the asymptotic behavior for $F(V,T)$ for $D_\alpha=1$ given by

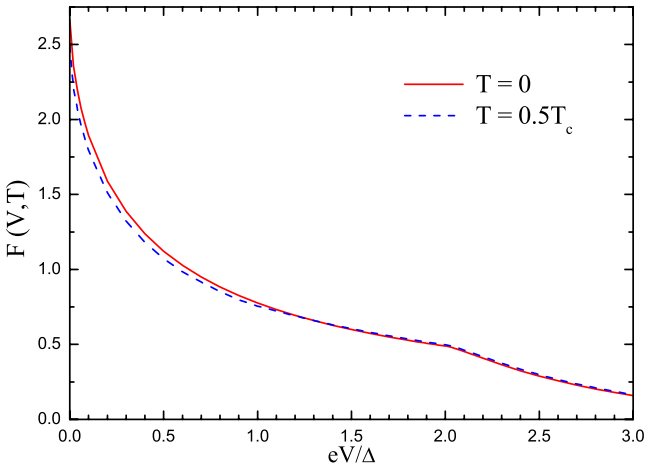

FIG. 13. (Color online) Dimensionless factor, $F(V,T)$, for the torque in Eq. (49) for $T=0$ and $T=0.5T_c$. $F(V,T)$ is inversely proportional to V for $eV \gg \Delta$.

$$F(V,T) \simeq 2\,\mathrm{Re}\int_{-\infty}^{+\infty}\frac{d\varepsilon}{\Delta}\langle x_3^K(\epsilon_1)\gamma_3^R(\epsilon_{-1})\tilde{\gamma}_1^R(\epsilon) - x_1^K(\epsilon)\gamma_1^R(\epsilon_2)\tilde{\gamma}_3^R(\epsilon_1)\rangle. \quad (50)$$

At zero temperature integration of Eq. (50) yields

$$\tau_{1s}(T=0) \simeq N_f v_f \mathcal{A}\Delta\hbar\frac{\Delta\ln 2}{eV}\langle\sin^2\vartheta\rangle\sin\psi, \quad (51)$$

and thus, the ac spin-transfer torque is inversely proportional to the voltage bias in the limit $eV \gg \Delta$.

In the opposite limit, $eV \ll \Delta$, the time evolution of spin-transfer torque is governed by the nearly adiabatic dynamics of the Andreev bound states. The spin-transfer torque, however, does not assume its instantaneous equilibrium value, i.e., $\vec{\tau}(t) \neq \vec{\tau}_{\mathrm{eq}}[\phi(t)]$. The reason is that the *dynamics* of the bound-state *spectrum*, i.e., $\epsilon_j^B[\phi(t)]$, leads to out of equilibrium population of the Andreev bound states. The occupation of the Andreev bound states remains constant as a function of time until the bound-state energy evolves to the gap edge at which point these states equilibrate with the continuum quasiparticles in the leads within a time scale much shorter than the period of a Josephson oscillation. This argument was made by Averin and co-workers[52,56] to describe the adiabatic time evolution of the charge transport in high transmission Josephson point contacts. To obtain the adiabatic limit for the dynamics of the spin-transfer torque, we replace the Fermi function $f(\epsilon_j)$ in Eq. (40) with $f(\pm\Delta)$. For $eV>0$ the Josephson phase φ increases with time. The phase dispersion of Andreev bound states given by Eq. (38) indicates that the occupation of bound states at energy $\epsilon_{\pm}^{<}[\phi(t)]$ is given by $f(\Delta)$, while the occupation of bound states at energy $\epsilon_{\pm}^{>}[\phi(t)]$ is given by $f(-\Delta)$. This procedure yields

$$\vec{\tau}^b(t) \simeq N_f v_f \mathcal{A}\Delta\pi\frac{\hbar}{2}\tanh\frac{\Delta}{2T}\left\langle\frac{\sin^2\vartheta}{\sin\chi}\left[\left|\sin\left(\frac{\chi}{2}+\omega t\right)\right| - \left|\sin\left(\frac{\chi}{2}-\omega t\right)\right|\right]\right\rangle\hat{\mathbf{x}}. \quad (52)$$

The time evolution of the torque, $\tau^b(t)$, at zero temperature is shown in Fig. 14 for $\psi=\pi/2$, $\vartheta=\pi/2$, and $\pi/4$. If we expand $\tau_b(t)$ in Fourier series, we find the sine part of the first Fourier component is $\tau_{1s}=\frac{4}{3}N_f v_f \mathcal{A}\Delta\hbar$ for $\psi=\vartheta=\pi/2$, which agrees with our numerical result in Fig. 13. It is clear that the higher-order Fourier components are nonzero, but their magnitudes are much smaller than τ_{1s}.

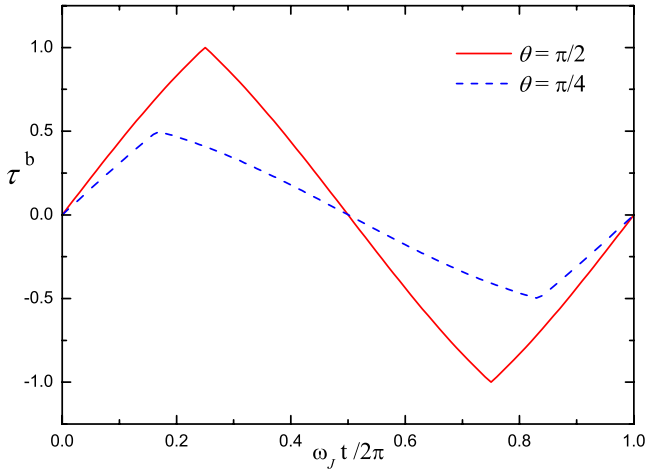

FIG. 14. (Color online) The time evolution of the spin-transfer torque on F^b in the adiabatic limit. $\psi=\pi/2$ and $T=0$. Although $\tau_{1s}\sin(\omega_J t)$ is the dominant term in the Fourier expansion of $\tau^b(t)$, the deviation from the $\sin(\omega_J t)$ dependence is obvious.

V. SUMMARY

In this paper we studied spin momentum transfer in superconducting nanopillars in the clean limit using models for the interface scattering matrices for the magnetic contacts. Our method presented in Sec. II, however, is quite general. Further exploration of the parameter space $\{D_\alpha, \vartheta, \psi\}$ as well as investigations on the effects of impurity scattering in the N spacer, spin-flip scattering at the ferromagnetic interfaces, etc. can be carried out within the current theoretical framework. The available information on the scattering parameters for SFNFS structures, e.g., the directional dependence of spin mixing angles, is a potential limitation. However, spin transport is dominated by trajectories close to normal incidence. For trajectories substantially away from the normal direction, e.g., the grazing trajectories $\Theta \sim \pi/2$, the effective thickness of the F layer is large and the transmission probability is very small. Their contribution to the total transport current is negligible even though the spin mixing might be strong. Therefore we believe that the basic features we obtain from our S-matrix models for the F interfaces, such as the out-of-plane torque and its nonlinear voltage dependence will survive the average over scattering trajectories for more detailed models for the interface S matrices. Indeed we expect our model to provide a good approximation for realistic device behavior.

In summary, we investigated the nonequilibrium spin-transfer torque in voltage-biased superconducting magnetic nanopillars. Our work extends earlier research on equilibrium phase-sensitive spin-transfer torque by Waintal and Brouwer[20] to nonequilibrium junctions. Our results, and the

general theoretical framework, provide a computational formalism for understanding the operation of nonequilibrium superconducting spin-transfer devices. We have shown that a superconducting nanopillar is an interesting system with new physics, particularly a rich dynamics resulting from the interplay of multiple Andreev reflection, spin mixing, spin filtering, spectral dynamics of the interface states, and the Josephson phase dynamics. The nonequilibrium torque at finite voltages is in principle observable by monitoring the magnetization dynamics, as described in Ref. 20. However, the details of the coupled magnetization dynamics and the time-dependent spin-transfer torque is a topic for a future study.

ACKNOWLEDGMENTS

We thank Tomas Löfwander for stimulating discussions on this work and for the diagram notation of the interface boundary conditions used in Sec. II.

APPENDIX: THE FOLDING PRODUCT

Our evaluation of folding products follows closely the pioneering work of Arnold.[43] Double-time correlation functions can be Fourier transformed between the time domain and the energy domain,

$$A(t_1,t_2)=\int_{-\infty}^{+\infty}\frac{d\epsilon'}{2\pi}\int_{-\infty}^{+\infty}\frac{d\epsilon''}{2\pi}e^{-i\epsilon' t_1}A(\epsilon',\epsilon'')e^{i\epsilon'' t_2}. \quad \text{(A1)}$$

The folding product is most conveniently evaluated in the energy domain,

$$[A\circ B](\epsilon',\epsilon'')=\int_{-\infty}^{+\infty}\frac{d\epsilon}{2\pi}A(\epsilon',\epsilon)B(\epsilon,\epsilon''). \quad \text{(A2)}$$

We can fix the condensate phase and electrical potential of the left electrode to be zero. It is easy to show that the matrix elements of incoming Riccati amplitudes in the electrodes are given by

$$\gamma_1^R(\epsilon',\epsilon)=2\pi\delta(\epsilon'-\epsilon)\gamma_1^R(\epsilon), \quad \text{(A3)}$$

$$x_1^K(\epsilon',\epsilon)=2\pi\delta(\epsilon'-\epsilon)x_1^K(\epsilon), \quad \text{(A4)}$$

$$\gamma_3^R(\epsilon',\epsilon)=2\pi\delta(\epsilon'-\epsilon+2\omega)\gamma_3^R(\epsilon-\omega), \quad \text{(A5)}$$

$$x_3^K(\epsilon',\epsilon)=2\pi\delta(\epsilon'-\epsilon)x_3^K(\epsilon+\omega). \quad \text{(A6)}$$

where $\omega=\omega_J/2$ and $\gamma^R(\epsilon)$ and $x^K(\epsilon)$ take their bulk equilibrium values.[26] The remaining Riccati amplitudes are obtained from those above by the symmetry relation, $\tilde{q}(\hat{p}_f,\epsilon',\epsilon)\equiv q^*(-\hat{p}_f,-\epsilon',-\epsilon)$. Note that γ_3^R and $\tilde{\gamma}_3^R$ are ladder operators in energy space, while the amplitudes $\gamma_1^R,\tilde{\gamma}_1^R,x_j^K$ and $\tilde{x}_j^K$ are diagonal in energy space.

Inspection of the boundary conditions, Eqs. (1)–(19), shows that all the coherence functions in the N layer, as well as all the effective scattering amplitudes (r,t,a) defined at F^a and F^b, have the form of

$$A(\epsilon',\epsilon)=\sum_{m=-\infty}^{+\infty}2\pi\delta(\epsilon'-\epsilon_m)A_{m0}(\epsilon), \quad \text{(A7)}$$

where we introduced the short-hand notation, $\epsilon_m\equiv\epsilon+m\omega$. This expansion reflects the fact that quasiparticles of energy ϵ are only scattered to sideband energies, $\{\epsilon_m\}$, during multiple Andreev reflection processes. Furthermore, the matrix elements of the distribution functions in the N layer are nonzero only between states corresponding to the sideband energies,

$$X(\epsilon',\epsilon'')=\sum_{m,k}\int\frac{d\epsilon}{2\pi}2\pi\delta(\epsilon'-\epsilon_{2m})2\pi\delta(\epsilon''-\epsilon_{2k})X_{2m,2k}(\epsilon). \quad \text{(A8)}$$

The integration variable ϵ provides a natural reference energy to introduce a discrete basis, $\{|m\rangle\equiv|\epsilon_m\rangle\}$, in energy space,[43]

$$\sum_m|m\rangle\langle m|=1,\quad A_{mn}(\epsilon)\equiv\langle m|A|n\rangle. \quad \text{(A9)}$$

In the Arnold basis, each spectral operator is represented by an infinite dimensional matrix, and the folding product reduces to matrix product,

$$[A\circ B]_{mn}(\epsilon)=\sum_k A_{mk}(\epsilon)B_{kn}(\epsilon). \quad \text{(A10)}$$

For general interface scattering matrices, the iteration algorithm described in Sec. II to solve the boundary conditions must be carried out numerically. To this end, we truncate the infinite dimensional matrices in energy space and work in a space of dimension $(2M+1)\times(2M+1)$. This corresponds to neglecting contributions from MAR processes with more than M reflections.[43] Usually $M>4$ yields sufficiently accurate results except for small voltages, e.g., $eV<0.1\Delta$.

Once the Riccati amplitudes are calculated using the iteration algorithm, we can assemble the Keldysh Green's functions to obtain the spin current, e.g., in the N layer,

$$\vec{I}^{(2)}(t,V)=N_f v_f A\pi\frac{\hbar}{2}\mathfrak{Re}\sum_{k=-M}^{M}\sum_{m}^{|k+m|\le M}e^{i2m\omega t}\times\int\frac{d\epsilon}{2\pi}\langle\mathrm{Tr}[\vec{\sigma}\mathrm{K}_{(k,k+m)}(\epsilon)]\rangle, \quad \text{(A11)}$$

where the kernel is given

$$\mathrm{K}_{(m,n)}(\epsilon)\equiv\frac{1}{2\pi i}\langle 2m|g_{2>}^K-g_{2<}^K|2n\rangle. \quad \text{(A12)}$$

The spin currents in the left and right electrodes, $\vec{I}^{(1)}(t)$ and $\vec{I}^{(3)}(t)$, are computed in similar fashions.

For transparent SFNFS point contacts, the spin current can be obtained analytically. In constructing the Keldysh Green's functions, the matrix elements of $(1-A)^{-1}$ are computed by expanding it in geometric series, $(1-A)^{-1}=\Sigma_{k=0}^{\infty}A^k$. For example, the probability amplitude of bulk quasiparticles being scattered from energy ϵ to $\epsilon+2k\omega$ via MAR is

$$M_k(\epsilon) = \langle 2k|(1-\Gamma_2^R \odot \tilde{\gamma}_2^R)^{-1}|0\rangle = \prod_{j=1}^{k} e^{i\sigma_z\vartheta/2}\gamma_1^R(\epsilon_{2j})e^{-i\sigma_z\vartheta/2}e^{-i\sigma'_\psi\vartheta/2}\tilde{\gamma}_3^R(\epsilon_{2j-1})e^{i\sigma_\psi\vartheta/2}. \tag{A13}$$

We adopt the convention $\Pi_{j=1}^{0}(\ldots)=1$ and $\Pi_{j=1}^{k>j}A_j = A_kA_{k-1}\ldots A_2A_1$. Besides M_k, the following transition amplitudes are required to construct $\hat{g}_{2>}^K$ and $\hat{g}_{2<}^K$,

$$N_k(\epsilon) = M_k(\epsilon)e^{i\sigma_z\vartheta/2}\gamma_1^R(\epsilon)e^{-i\sigma_z\vartheta/2}, \tag{A14}$$

$$O_k(\epsilon) = \prod_{j=1}^{k} e^{i\sigma_\psi\vartheta/2}\gamma_3^R(\epsilon_{-2j+1})e^{-i\sigma'_\psi\vartheta/2}e^{-i\sigma_z\vartheta/2} \times \tilde{\gamma}_1^R(\epsilon_{-2j+2})e^{i\sigma_z\vartheta/2}, \tag{A15}$$

$$P_k(\epsilon) = O_k(\epsilon)e^{i\sigma_\psi\vartheta/2}\gamma_3^R(\epsilon_1)e^{-i\sigma_{-\psi}\vartheta/2}. \tag{A16}$$

The magnitudes of these amplitudes decay rapidly with increasing MAR order, i.e., k, as well as the bias voltage. The spin current in the N layer is found to be

$$\vec{I}^{(2)}(t,V) = N_f v_f \mathcal{A}\pi\frac{\hbar}{2}\Re\mathfrak{e}\sum_{m=-\infty}^{+\infty}\sum_{k=0}^{\infty}e^{i2m\omega t} \times \int\frac{d\epsilon}{2\pi}\langle \mathrm{Sp}[\vec{\sigma}\mathrm{K}_{(k,m)}(\epsilon)]\rangle,$$

$$\mathrm{K}_{(k,m)} = N_k(\epsilon)\tilde{x}_3^K(\epsilon_{-1})N_{k+m}^\dagger(\epsilon) - M_k(\epsilon)x_1^K(\epsilon)M_{k+m}^\dagger(\epsilon) + O_k(\epsilon)x_3^K(\epsilon_1)O_{k-m}^\dagger(\epsilon) - P_k(\epsilon)\tilde{x}_1^K(\epsilon_2)P_{k-m}^\dagger(\epsilon). \tag{A17}$$

$\vec{I}^{(1)}$ and $\vec{I}^{(3)}$ have the same form as Eq. (A17) but with slightly different definitions of the transition amplitudes $\{M_k, N_k, O_k, P_k\}$.

[1] J. C. Slonczewski, J. Magn. Magn. Mater. **159**, L1 (1996).
[2] L. Berger, Phys. Rev. B **54**, 9353 (1996).
[3] A. Brataas, G. E. W. Bauer, and P. Kelly, Phys. Rep. **427**, 157 (2006).
[4] D. C. Ralph and M. D. Stiles, J. Magn. Magn. Mater. **320**, 1190 (2008).
[5] M. Tsoi, A. G. M. Jansen, J. Bass, W.-C. Chiang, M. Seck, V. Tsoi, and P. Wyder, Phys. Rev. Lett. **80**, 4281 (1998).
[6] E. B. Myers, D. C. Ralph, J. A. Katine, R. N. Louie, and R. A. Buhrman, Science **285**, 867 (1999).
[7] S. I. Kiselev, J. C. Sankey, I. N. Krivorotov, N. C. Emley, R. J. Schoelkopf, R. A. Buhrman, and D. C. Ralph, Nature (London) **425**, 380 (2003).
[8] I. N. Krivorotov, N. C. Emley, J. C. Sankey, S. I. Kiselev, D. C. Ralph, and R. A. Buhrman, Science **307**, 228 (2005).
[9] J. C. Slonczewski, Phys. Rev. B **39**, 6995 (1989).
[10] J. E. Ortega and F. J. Himpsel, Phys. Rev. Lett. **69**, 844 (1992).
[11] M. D. Stiles, Phys. Rev. B **48**, 7238 (1993).
[12] P. Bruno, Phys. Rev. B **52**, 411 (1995).
[13] P. Grünberg, R. Schreiber, Y. Pang, M. B. Brodsky, and H. Sowers, Phys. Rev. Lett. **57**, 2442 (1986).
[14] S. S. P. Parkin, N. More, and K. P. Roche, Phys. Rev. Lett. **64**, 2304 (1990).
[15] A. Brataas, Y. V. Nazarov, and G. E. W. Bauer, Phys. Rev. Lett. **84**, 2481 (2000).
[16] X. Waintal, E. B. Myers, P. W. Brouwer, and D. C. Ralph, Phys. Rev. B **62**, 12317 (2000).
[17] C. Heiliger, M. Czerner, B. Yu. Yavorsky, I. Mertig, and M. D. Stiles, J. Appl. Phys. **103**, 07A709 (2008).
[18] M. D. Stiles and A. Zangwill, Phys. Rev. B **66**, 014407 (2002).
[19] X. Waintal and P. W. Brouwer, Phys. Rev. B **63**, 220407(R) (2001).
[20] X. Waintal and P. W. Brouwer, Phys. Rev. B **65**, 054407 (2002).
[21] C. Bell, G. Burnell, C. W. Leung, E. J. Tarte, D.-J. Kang, and M. G. Blamire, Appl. Phys. Lett. **84**, 1153 (2004); IEEE Trans. Appl. Supercond. **15**, 908 (2005).
[22] N. Schopohl and K. Maki, Phys. Rev. B **52**, 490 (1995).
[23] N. Schopohl, arXiv:cond-mat/9804064 (unpublished).
[24] M. Eschrig, J. A. Sauls, and D. Rainer, Phys. Rev. B **60**, 10447 (1999).
[25] A. Shelankov and M. Ozana, Phys. Rev. B **61**, 7077 (2000).
[26] M. Eschrig, Phys. Rev. B **61**, 9061 (2000).
[27] J. W. Serene and D. Rainer, Phys. Rep. **101**, 221 (1983).
[28] J. Rammer and H. Smith, Rev. Mod. Phys. **58**, 323 (1986).
[29] A. V. Zaitsev, Sov. Phys. JETP **59**, 1015 (1984).
[30] G. Kieselmann, Ph.D. thesis, University of Bayreuth, 1985.
[31] A. Millis, D. Rainer, and J. A. Sauls, Phys. Rev. B **38**, 4504 (1988).
[32] J. C. Cuevas and M. Fogelström, Phys. Rev. B **64**, 104502 (2001).
[33] J. Kopu, M. Eschrig, J. C. Cuevas, and M. Fogelström, Phys. Rev. B **69**, 094501 (2004).
[34] T. M. Klapwijk, G. E. Blonder, and M. Tinkham, Physica B & C **109-110**, 1657 (1982).
[35] W. T. Reid, *Riccati Differential Equations* (Academic, New York, 1972).
[36] E. Zhao, T. Löfwander, and J. A. Sauls, Phys. Rev. B **70**, 134510 (2004).
[37] M. Fogelström, Phys. Rev. B **62**, 11812 (2000).
[38] M. Ashida, S. Aoyama, J. Hara, and K. Nagai, Phys. Rev. B **40**, 8673 (1989).
[39] A. Brinkman and A. A. Golubov, Phys. Rev. B **61**, 11297 (2000).
[40] A. V. Galaktionov and A. D. Zaikin, Phys. Rev. B **65**, 184507 (2002).
[41] M. Ozana, A. Shelankov, and J. Tobiska, Phys. Rev. B **66**, 054508 (2002).
[42] A. Brinkman, A. A. Golubov, H. Rogalla, F. K. Wilhelm, and M. Yu. Kupriyanov, Phys. Rev. B **68**, 224513 (2003).
[43] G. B. Arnold, J. Low Temp. Phys. **68**, 1 (1987).
[44] K. Xia, M. Zwierzycki, M. Talanana, P. J. Kelly, and G. E. W. Bauer, Phys. Rev. B **73**, 064420 (2006).

[45] The phase factor φ eventually drops out in the calculation, see discussion in Sec. V and Ref. 20.
[46] Yu. S. Barash, I. V. Bobkova, and T. Kopp, Phys. Rev. B **66**, 140503(R) (2002).
[47] Y. Tserkovnyak, A. Brataas, G. E. W. Bauer, and B. I. Halperin, Rev. Mod. Phys. **77**, 1375 (2005).
[48] T. Tokuyasu, J. A. Sauls, and D. Rainer, Phys. Rev. B **38**, 8823 (1988).
[49] C. J. Lambert and R. Raimondi, J. Phys.: Condens. Matter **10**, 901 (1998).
[50] W. Belzig, F. K. Wilhelm, C. Bruder, G. Schön, and A. Zaikin, Superlattices Microstruct. **25**, 1251 (1999).
[51] E. N. Bratus', V. S. Shumeiko, and G. Wendin, Phys. Rev. Lett. **74**, 2110 (1995).
[52] D. V. Averin and A. Bardas, Phys. Rev. Lett. **75**, 1831 (1995).
[53] J. C. Cuevas, A. Martin-Rodero, and A. L. Yeyati, Phys. Rev. B **54**, 7366 (1996).
[54] A. V. Zaitsev and D. V. Averin, Phys. Rev. Lett. **80**, 3602 (1998).
[55] M. Andersson, J. C. Cuevas, and M. Fogelström, Physica C **367**, 117 (2002).
[56] D. Averin and A. Bardas, Phys. Rev. B **53**, R1705 (1996).